Progress In Electromagnetics Research, PIER 68, 317–337, 2007

SIMULTANEOUS TIME-FREQUENCY MODELING OF ULTRA-WIDEBAND ANTENNAS BY TWO-DIMENSIONAL HERMITE PROCESSING

G. Marrocco, M. Migliorelli, and M. Ciattaglia

Dipartimento di Informatica Sistemi e Produzione
Universita' di Roma Tor Vergata
Via del Politecnico, 1, 00133 Roma (RM), Italy

Abstract—This paper proposes an approximate space-time-frequency field representation for directive Ultra-wideband antennas useful to be introduced into a system-level evaluation tool. Based on the observation that the very near field collected on a plane close to the antenna exhibits a compact support, such a field is processed in the time domain by the two-dimensional Hermite transform. This approach permits to simultaneously express the antenna impulse response and the transfer function by semi-analytical formulas. The theory is demonstrated by numerical examples which highlights that good representations of complex antennas can be achieved by a small set of associate Hermite functions.

1. INTRODUCTION

Recent advances in Ultra -wideband (UWB) systems and applications [1, 23] are producing renewed interest in the development and modeling of impulse-like radiating antennas. Although modern numerical tools permit to achieve a detailed fullwave analysis of the antenna in both the time and the frequency domains [24], it is emerging the need of smart space-time-frequency representations able to describe the complex antenna dynamics by a small set of parameters. This topic is of particular relevance when the antenna description has to be introduced into a system-level evaluation tool which requires the application of ray tracing for the modeling of indoor propagation or the antenna interaction with any other kind of scatterer. In previous papers [2, 3] the authors have proposed space-time-frequency interpolating functions for the efficient representation of the antenna impulse response or transfer function in the case of aperture radiators

such as slots, open-ended waveguides and horns of rectangular and circular shapes. The waveguide eigenvectors are used as space-varying basis functions for aperture field representation, while the time dependence is interpolated over a set of complex exponentials. For antennas of more general shapes, such as UWB dipoles, TEM horn and non canonical-aperture horns [24, 25], different kinds of entire-domain basis functions need to be considered.

This paper addresses a compact UWB field representation employing the two-dimensional Associate Hermite Functions (AHF2). This base has been already introduced many years ago for the modeling of optical resonators and beam-waveguides [4–6] and then applied for radiative problems in the quasi-optical region for the analysis of hexagonal and diagonal horns [7, 8] and in the microwave region for the frequency-domain modeling of large apertures [9] exploiting the possibility to approximately calculate the Fresnel and Fraunhofer radiation by simple formulas. In [10] one-dimensional Associate Hermite Functions are used to characterize the modes of dielectric waveguides. More recently [11] one-dimensional AH Functions have applied to extrapolate both time and frequency domain electromagnetic responses of structures using early-time and low-frequency simulation data. Further interesting multiscale applications can be found in [12] where the Hermite formalism was adopted for image coding and computer visual systems.

Such a base is here applied to time-varying electromagnetic images, by means of an automatic a-priori choice of the most critical parameters such as the scaling factors. The model is useful for directive antennas, but it is much more general than the model involving an aperture on an infinite screen.

After the basic formulation for impulse response and transfer function of UWB antennas in Section 2, the basic theory of the near-field processing is developed in Section 3 followed by some computation issues in Section 4 addressing the automatic choice of the relevant processing parameters. The method is finally demonstrated with some examples in Section 5.

2. STATEMENT OF THE PROBLEM

The antenna impulse response $\boldsymbol{h}^T(\hat{\boldsymbol{r}}, \tau)$, e.g., the transmitting-mode effective height is formally obtained as the Radon transform of the antenna current corresponding to a feeding Dirac voltage pulse [14]. In the frequency domain the transfer function $\boldsymbol{\mathcal{H}}(\hat{\boldsymbol{r}}, \omega)$, which is directly related to the realized gain (and hence includes the antenna-source mismatch), is the Fourier transform of the time domain effective

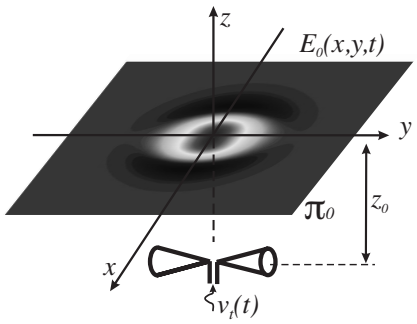

Figure 1. The relevant geometry for the Hermite processing of a time-varying near field.

height. An approximation, commonly adopted in the measurement context, replaces the knowledge of the antenna current with the field on a plane, say π_0 of normal vector $\hat{\boldsymbol{z}}$, placed at close proximity to the antenna (Fig. 1). Relevant far field functions, such as the impulse response and the transfer function (proportional to the far field radiated by the antenna, sourced by an impulsive excitation, in the time- and frequency-domain respectively), are then obtained by a two-dimensional Radon transform (time-domain) [15] or spectral Fourier transform (frequency domain) as

$$\boldsymbol{h}^T(\hat{\boldsymbol{r}},\tau) = -\frac{2}{\eta_0}\hat{\boldsymbol{r}} \times \iint\limits_{\pi_0} \boldsymbol{E}_0^{\delta}\left(\boldsymbol{\rho}, \tau + \frac{\hat{\boldsymbol{r}}\cdot\boldsymbol{\rho}}{c}\right) ds \times \hat{\boldsymbol{z}} * \delta^{(1)}(\tau) \quad (1)$$

$$\boldsymbol{\mathcal{H}}(\hat{\boldsymbol{r}},\omega) = -2\frac{j\omega}{\eta_0}\hat{\boldsymbol{r}} \times \iint\limits_{\pi_0} \tilde{\boldsymbol{E}}_0^{\delta}(\boldsymbol{\rho},\omega) e^{j\frac{\omega}{c}\hat{\boldsymbol{r}}\cdot\boldsymbol{\rho}} ds \times \hat{\boldsymbol{z}} \quad (2)$$

where '*' means convolution, the symbol '*tilde*' denotes the Fourier transform between $t \to \omega$, $\tau = t - r/c$, domains, $\delta^{(1)}(\tau)$ is the first-derivative operator, $\boldsymbol{E}_0^{\delta}(\boldsymbol{\rho}, t)$ with $\boldsymbol{\rho} = x\hat{\boldsymbol{x}}, y\hat{\boldsymbol{y}} \in \pi_0$, is the time-varying electric tangential field on π_0 in the front of the antenna corresponding to a Dirac voltage pulse entering the antenna terminals. The latter function may be generally obtained by means of any time domain fullwave solver or by measurements. Since the antenna current is replaced by the field on a plane in front of the antenna, such a representation obviously represents the antenna dynamics only in $z > 0$ (or $z < 0$) half space and it is really accurate only for directive antennas. Further approximations truncate the integration within a finite region of π_0 in the front of the antenna.

Equations (1) and (2) need to be generally computed numerically except for very simple antenna geometries, involving a lengthy and time-consuming process. The computation requires the application of a local method, such as the Finite-Difference Time-Domain (FDTD) [16], to calculate the aperture field when the antenna is sourced by a broadband test signal, since the Dirac pulse is not suitable as input signal for numerical codes. The corresponding field on the π_0 plane needs to be stored within the whole transient and numerical deconvolution is then applied to each radiating pixel to calculate $\boldsymbol{E}_0^{\delta}$. Finally, the impulse response and transfer functions are obtained by numerical evaluation of surface integral in (1) and (2) which has to be repeated at any required time (frequency) and observation direction because of the coupling between angular and spatial variables. A complete broadband antenna characterization over the whole radiating angle is therefore a time-consuming computational task.

Nevertheless the authors have shown in previous papers how such integrals can be calculated analytically provided that the near field is interpolated over proper time-independent functions having known Fourier transform. The problem was solved for aperture-radiating antennas of canonical shapes where the interpolating functions can be chosen as the eigenvectors of rectangular or circular waveguides having the same cross-section of the aperture. This representation does not fit other kind of antennas and hence more general interpolating functions need to be introduced.

3. HERMITE PROCESSING OF THE TIME-VARYING FIELD

Provided that the plane π_0 (Fig. 1) is placed at a close proximity to the antenna, the electric (or also the magnetic) field will be mostly concentrated within a small region of π_0. In other words we can suppose that the near field exhibits a compact support on π_0. Under this hypothesis, an efficient choice for the interpolating basis is the two-dimensional Associate Hermite Functions (hereafter denoted as AHF2) defined as

$$h_{mn}(x, y, w_x, w_y) = \frac{1}{\sqrt{\pi w_x w_y}\sqrt{2^{m+n} m! n!}} H_m\left(\frac{x}{w_x}\right) H_n\left(\frac{y}{w_y}\right) e^{-\left(\frac{x^2}{2w_x^2}+\frac{y^2}{2w_y^2}\right)} \tag{3}$$

Here $H_m(\xi)$ is the mth Hermite polynomial. AHF2s (Fig. 2) form a scalar orthonormal basis, they are spatially separable and show a compact support around $(x = 0, y = 0)$ which can be controlled by

the scaling factors $\{w_x, w_y\}$. Even functions, such as h_{00}, are useful to represent the co-polar field component, while the cross-polar is modeled by odd functions, for instance h_{11}. As the functions order (n, m) increases, the resulting support enlarges. The extreme values of a Hermite function exhibits near equal amplitudes which is a rather useful feature to model close-to-the-edge field singularities and large radiating objects such as arrays.

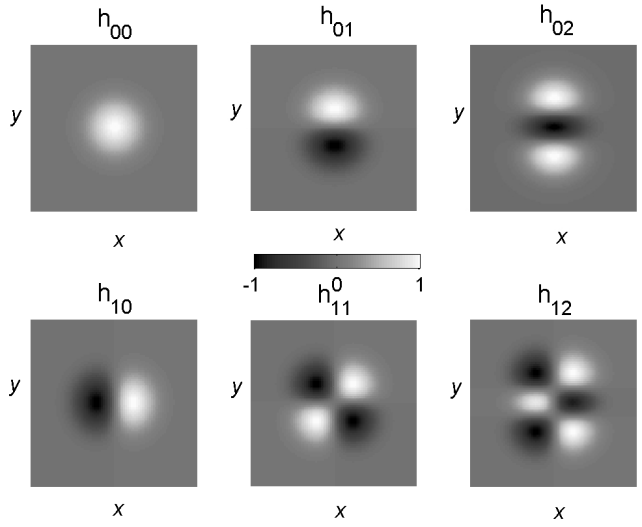

Figure 2. Some two-dimensional Associate Hermite functions having equal scaling factors $w_x = w_y$.

Beside this choice, also the Hermite Rodriguez functions [17] could be considered for the interpolation of compact-support images, but it has been verified that the corresponding interpolation converges not uniformly and slower [12] than the AHF2 and that the interpolation accuracy is more sensible to the scale factor than in the case of AHF2.

The AHF2 share the same properties of the more conventional 1D associate Hermite functions and, in particular they are isomorphic with their Fourier transform, e.g.,

$$\int_{-\infty}^{+\infty}\int_{-\infty}^{+\infty} h_{mn}(x, y, w_x, w_y)e^{-j2\pi(\xi x+\eta y)}dxdy = (-j)^{m+n}h_{mn}(\xi, \eta, \tfrac{1}{2\pi w_x}, \tfrac{1}{2\pi w_y}) \quad (4)$$

The time-varying coefficients $\boldsymbol{g}_{mn}(\tau) = g_{x,mn}(\tau)\hat{\boldsymbol{x}} + g_{y,mn}(\tau)\hat{\boldsymbol{y}}$ for

the near field approximation

$$\boldsymbol{E}_0^{\delta}(x,y,t) \simeq \sum_{m,n=0}^{N} \boldsymbol{g}_{mn}(\tau) h_{mn}(x,y,w_x,w_y) \tag{5}$$

are formally defined as the *two-dimensional Hermite transform* of the impulsive aperture field on π_0

$$\boldsymbol{g}_{mn}(\tau) = \iint_{\pi_0} \boldsymbol{E}_0^{\delta}(x,y,\tau) h_{mn}(x,y,w_x,w_y) dxdy \tag{6}$$

3.1. Transfer Function

According to expansion in (5), and thanks to the isomorphism in (4), it is easy to show that the antenna transfer function is given by

$$\boldsymbol{\mathcal{H}}^T(\hat{\boldsymbol{r}},\omega) \simeq -2\frac{j\omega}{\eta_0}\hat{\boldsymbol{r}} \times \sum_{m,n=0}^{N} \tilde{\boldsymbol{g}}_{mn}(\omega) F_{mn}(k_x,k_y) \times \hat{\boldsymbol{z}} \tag{7}$$

The plane wave spectrum of the mnth AHF2 is

$$F_{mn}(k_x,k_y) = (-j)^{m+n} h_{mn}(-\frac{k_x}{2\pi}, -\frac{k_y}{2\pi}, \frac{1}{2\pi w_x}, \frac{1}{2\pi w_y}) \tag{8}$$

with $k_x = \frac{\omega}{c}\hat{\boldsymbol{r}} \cdot \hat{\boldsymbol{x}}$ and $k_y = \frac{\omega}{c}\hat{\boldsymbol{r}} \cdot \hat{\boldsymbol{y}}$.

Only the portion of $F_{mn}(k_x,k_y)$ in the visible space $|k_{x,y}| \leq \omega/c$ will contribute to the radiated fields. Fig. 3 shows some examples of F_{mn} plots in spherical coordinates at some frequencies. Increase in the order (m,n) yields a larger number of lobes, while increasing the frequency forces the lobes to move toward the broadside. At the purpose to regenerate the whole frequency-domain antenna dynamics, the expansion coefficients, $\{\tilde{\boldsymbol{g}}_{mn}(\omega)\}$, are therefore the only data to store, rather than the whole transient near field. Moreover, as it will be recalled in the next paragraph, a further data compression can be achieved by pole-residue processing.

3.2. Impulse Response

Denoting with S_{π_0} the compact support of $\boldsymbol{E}_0^{\delta}(x,y,t)$ on the π_0 plane, for instance a circle of $\rho_{\max}$ radius, the time-domain effective height can be approximated [15] for signals with maximum frequency $f_{\max} \leq \rho_{\max}/c$ in terms of the plane-wave spectrum of each AHF2 pattern evaluated at the singular values of its own time-variant expansion

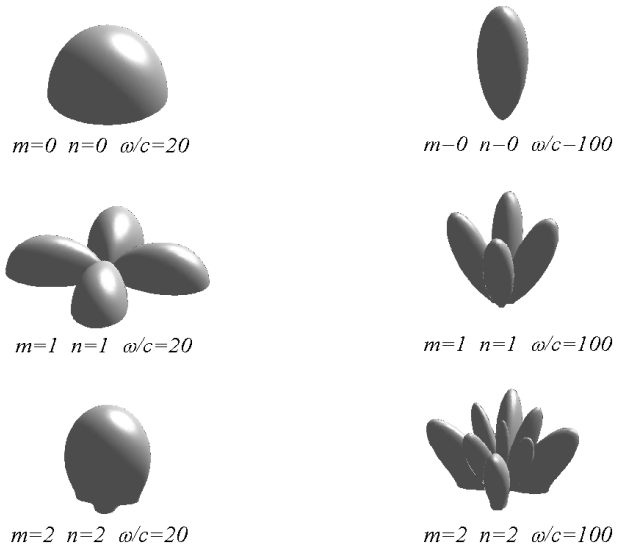

Figure 3. Examples of the $k-$domain AHF2 functions $|h_{mn}(-\frac{k_x}{2\pi}, -\frac{k_y}{2\pi}, \frac{1}{2\pi w_x}, \frac{1}{2\pi w_y})|$ of different orders plotted at some frequencies in angular coordinates (θ, ϕ).

coefficients. Therefore, denoting for instance with $\{s_{x,mnk}, g_{x,mnk}\}$ the pole-residue signature of the $g_{x,mn}(\tau)$ function, e.g., such that $g_{x,mn}(\tau) \simeq \sum_k g_{x,mnk} e^{s_{x,mnk}\tau}$, the $x-$ component of the TD effective height is given by

$$h_x^T(\hat{\boldsymbol{r}}, \tau) \simeq= -2\frac{1}{\eta_0}\hat{\boldsymbol{r}} \times$$
$$\sum_{m,n=0}^{N} \sum_{k=0}^{K_{mn}} T_{x,mnk} h_{mn}(\frac{j s_{x,mnk}}{2\pi c} r_x, \frac{j s_{x,mnk}}{2\pi c} r_y, \frac{1}{2\pi w_x}, \frac{1}{2\pi w_y}) e^{s_{x,mnk}\tau} \quad (9)$$

where $T_{x,mnk} = (-j)^{m+n} s_{x,mnk} g_{x,mnk}$, and $r_x = \hat{\boldsymbol{r}} \cdot \hat{\boldsymbol{x}}$ and $r_y = \hat{\boldsymbol{r}} \cdot \hat{\boldsymbol{y}}$. The pole-residue processing has the additional advantage to produce both time- and frequency-models of the UWB antenna by the same set of data since $\tilde{g}_{x,mn}(\omega) = \sum_k \frac{g_{x,mnk}}{j\omega - s_{x,mnk}} e^{-j\omega + s_{x,mnk} z_0/c}$.

4. COMPUTATIONAL ISSUES

Since the Dirac pulse is not suited as input signal for numerical tools, a practically band-limited test signal $v_t(t)$, such as a Gaussian or

derivated-Gaussian pulse, is considered for the computation of the time-varying near field $\boldsymbol{E}_0(x, y, t)$ on π_0. Denoting with $\{v_{mn}(t)\}$ the Hermite transform of $\boldsymbol{E}_0$ as in (6), the required $\{g_{mn}(\tau)\}$ coefficients of $\boldsymbol{E}_0^{\delta}$ are then obtained from $\{v_{mn}(t)\}$ by deconvolutions as explained in [18] and in [15]. The pole-residue extraction can be executed by the Matrix Pencil method [19].

A critical task in the field approximation over the AHF2 set is the choice of the scaling factors $\{w_x, w_y\}$ which generally depends on the local scene context and strongly affects the expansion accuracy and efficiency. According to the theory in [9], a good rule to optimize the choice of the scale factor is that the radiated power of the interpolated distribution best matches the radiated power of the real field distribution. However this strategy is an *a-posteriori* one, since it requires the knowledge of the whole near-field dynamic and therefore it is not suitable to be incorporated into a time-domain solver for a run-time execution. Instead, it is desirable an *a-priori* selection of the scale factors which is related to the observable geometrical parameters, such as the antenna size and the distance between the antenna and the near-field observation plane. Since the support of $\boldsymbol{E}_0^{\delta}$ enlarges as the π_0 plane moves far from the antenna, at least in the near field, a robust *a-priori* choice of the scaling factor requires to account for both the antenna size and the distance z_0 from the expansion plane. At this purpose it is preliminarily defined an *effective antenna footprint* L_{eff} on π_0 under the simplifying hypothesis of spherical-wave radiation mechanism from the antenna edges (see Fig. 4).

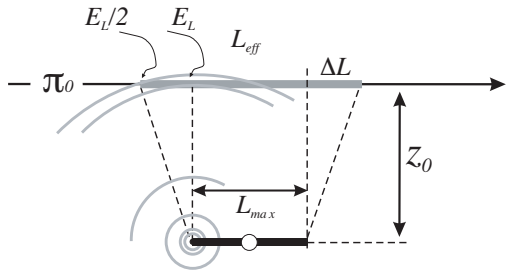

Figure 4. Geometry for the definition of the *antenna effective footprint* L_{eff} on π_0 according to a spherical radiation model from the antenna edges. E_L is the field amplitude on π_0 at the projections of the antenna boundary.

Denoting with $\Delta l \simeq 2z_0$ the distance on the π_0 plane between the projection of the antenna boundary and the point where the spherical wave emerging from the antenna edges attenuates to one half

its maximum amplitude, it is posed

$$L_{eff}(z_0) = L_{\max} + 4z_0 \tag{10}$$

It is here assumed that the scaling factor is a function of the sole L_{eff}. Among several options, it was experimentally found that a good choice can be

$$w_x = w_y = \frac{\lambda_{\min}}{4} \log\left(10\frac{L_{eff}}{\lambda_{\min}}\right) \tag{11}$$

where $\lambda_{\min}$ is the lowest frequency in the modeling. Under this assumption the accuracy of the Hermite expansion is rather insensitive to the position of the π_0 plane as it will be shown in the Examples Section.

The Hermite Transformation integrals in (6) theoretically extend to infinity, however near-field data are available only within a finite sub-domain of π_0. Such a truncation of the observation domain yields a limitation on the order of those AHF2s which can be retained in the field interpolation since the support of each AHF2 is roughly bounded by the first and the last roots of the corresponding Hermite polynomial and enlarges along with the function order. The following argument may be followed. An accurate strategy to numerically compute the Hermite transform in (6) could be the N-points Gauss-Hermite integration rule [21]

$$\int_{-\infty}^{+\infty} f(u)e^{-u^2}du \simeq \sum_{j=1}^{N} A_j f\left(u_j^{(N)}\right) \tag{12}$$

where $\{u_j^{(N)}\}$ are the roots of the Nth order Hermite polynomial and $\{A_j\}$ are proper integration weights. By applying this formula to (6), and accounting for the presence of scaling factors, it is easy to show that

$$\boldsymbol{g}_{mn}(\tau) \simeq \sum_{i=1}^{M}\sum_{j=1}^{N} A_i A_j \left[\boldsymbol{E}_0^{\delta} h_{mn} e^{\frac{x^2}{2w_x^2}+\frac{y^2}{2w_y^2}}\right]_{\substack{x=\sqrt{2}w_x u_i^{(M)} \\ y=\sqrt{2}w_y u_j^{(N)}}} \tag{13}$$

In order to apply the above formula to a truncated $L_0 \times L_0$ domain, $(-\frac{L_0}{2} \leq x, y \leq \frac{L_0}{2})$, all the required roots need to lay within that region. Therefore the highest-order, N and M, of AHF2s are such that the largest roots of the corresponding Hermite polynomials are

constrained to

$$u_i^{(M)} \leq \frac{L_0}{2\sqrt{2}w_x} \qquad u_j^{(N)} \leq \frac{L_0}{2\sqrt{2}w_y} \tag{14}$$

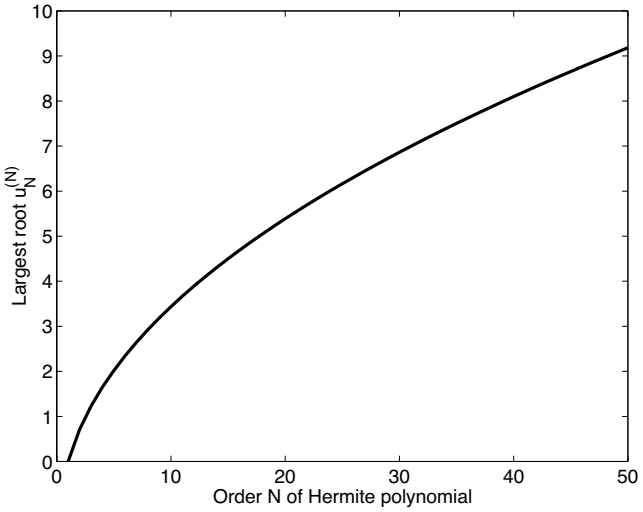

Figure 5. Largest roots $u_N^{(N)}$ of the Hermite polynomials $H_N(u)$.

Figure 5 shows the largest roots of the first $N = 50$ orders Hermite polynomials. Due to the non linearity of the curve, the number of Hermite functions to be retained in the near field interpolation is as more sensible to the size of the observation region as this becomes larger (e.g., roughly for $u_N^{(M)} > 5$). In other words, the roots come closer (approach) as the order of Hermite function increases.

Another well investigated consequence [20] of the observation region truncation is that the far field data are meaningful only within the solid angle formed by the edges of the antenna and the edge of the finite observation region. By parametrizing the size L_0 of near-field data domain on π_0 as $L_0 = L_{eff} + 2pz_0$ (p is an integer number), the antenna transfer function $\boldsymbol{\mathcal{H}}^T(\hat{\boldsymbol{r}}, \omega)$ will be considered only for angles $-\theta_0 \leq \theta \leq \theta_0$ where θ_0 is such that $\tan\theta_0 = \frac{L_0 - L_{\max}}{2z_0} = (p+2)$. From this formula it is possible to select the size of the numerical computation region in order to obtain the desired angular domain of the transfer function.

5. NUMERICAL EXAMPLES

The applicability and the accuracy of the method are now investigated with reference to two examples with different angular spreading of the radiated field, e.g., an aperture-type antenna, and an UWB planar dipole-like antenna.

In both the examples, time-varying relevant fields for the 2D Hermite transform are computed by a FDTD tool. Far-field solutions obtained with the proposed model will be compared with a reference solution obtained by an independent FDTD simulation whose computational domain is large enough to include some field test points in front of the π_0 plane. Differences among reference fields ($\boldsymbol{E}_1$) and reconstructed fields ($\boldsymbol{E}_2$) by the Associate Hermite functions are discussed according to the normalized root mean square (r.m.s.) error $\varepsilon(E_1, E_2) = \sqrt{||E_1 - E_2\|_2/\|E_1\|_2}$, (with $\|\cdot\|_2$ denoting the L_2 norm respect to (x, y) coordinates).

5.1. Aperture-radiating Antenna

A reference ultra-wideband ridged horn (CRH) antenna having (4 GHz–10 GHz) band, already used as a test case in previous papers [3], is here considered.

The test signal to stimulate the antenna response in the required band is a Gaussian pulse $v_t(t) = V_0 \exp[\frac{-(t-\tau_0)^2}{2T_0^2}]$ with parameters, $V_0 = 1V$, $T_0 = 35\,\text{ps}$ and $\tau_0 = 200\,\text{ps}$. The π_0 plane is placed at a distance $z_0 = 2.1\,\text{cm}$ from the horn aperture (corresponding to half a wavelength in the mid-band). The maximum size of the aperture is $L_{\max} = 10.5\,\text{cm}$ and therefore the effective aperture footprint on π_0 computed by (10) is $L_{eff} \simeq 19\,\text{cm}$. The observation region on π_0, e.g., the domain where the antenna near-field will be processed, is a square of side $L_0 \simeq 2L_{\max}$. Under this choice, the transfer function could be virtually computed within the angular domain $|\theta| < 68°$.

The near field energy, e.g., the L_2 norm respect to time, $e(x, y) = \|\boldsymbol{E}(\cdot, t)\|_2$, is expected to be well concentrated over the expansion plane π_0 right in front of the aperture (Fig. 6).

The scaling factors for the Hermite processing are chosen according to (11) as $w_x = w_y = 3.1\,\text{cm}$. In this case it is shown in Fig. 7 that the relative mean square error of the reconstructed field $\boldsymbol{E'}_0(x, y, t) \simeq \sum_{m,n=0}^{N} \boldsymbol{v}_{mn}(\tau) h_{mn}(x, y, w_x, w_y)$ compared with the original field $\boldsymbol{E}_0(x, y, t)$ is rather insensitive to the position z_0 of the observation plane. The authors experienced that the same condition roughly holds also for different kinds of antennas.

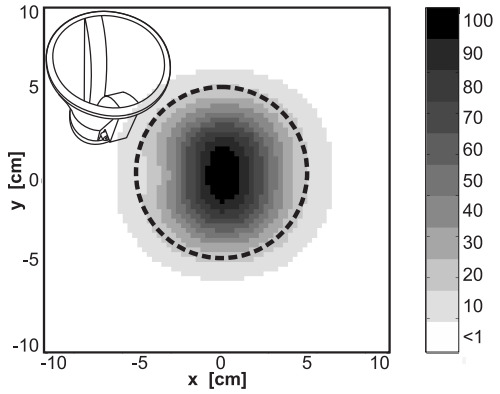

Figure 6. Normalized energy $e(x, y) = \|\boldsymbol{E}(\cdot, t)\|_2$ radiated by the circular ridged horn on the plane π_0 placed at distance $z_0 = 2.1\,\text{cm}$ from the antenna aperture. The circle indicates the antenna rim projection over π_0.

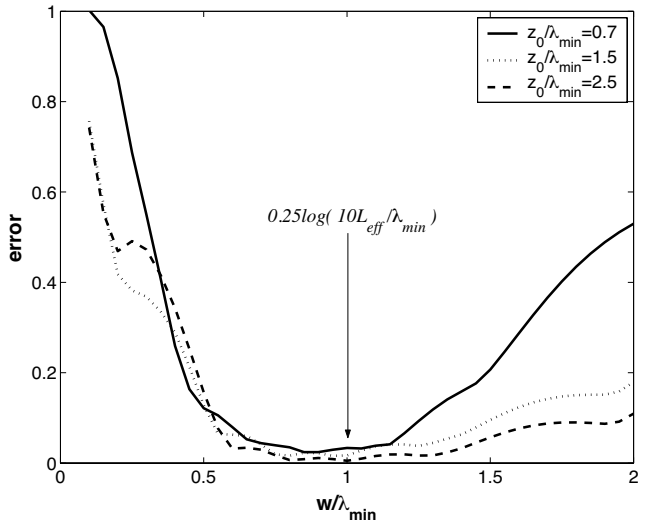

Figure 7. CRH antenna: reconstruction r.m.s. error $\varepsilon(E_{0,y}, \sum_{m,n} v_{y,mn} h_{mn,y})$, at time $t = 0.75\,\text{ns}$ vs. the scaling factor $w_x = w_y = w$ for different distances z_0 of the observation plane to the antenna and therefore of the effective antenna footprint L_{eff} on π_0. In this case $\lambda_{\min} = 3\,\text{cm}$.

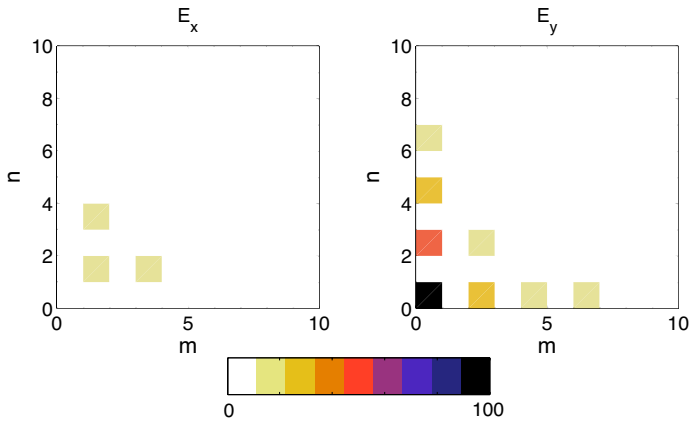

Figure 8. CRH antenna: energy spectrum of the Hermite coefficients for the field interpolation on π_0.

The energy spectrum $\|v_{x,mn}(\tau)\|_2$ of the Hermite coefficient for E_{0x} and E_{0y} components of orders $n, m \leq 10$ (Fig. 8) shows a chessboard-like distribution, interleaved among x- and y-components, with a high localization of the mostly excited AHF2s in the lower part of the band (small n and m). In particular, h_{00} and h_{11} functions dominate for y- (co-polar) and x-components (cross-polar) respectively. By considerations in Section 4 (see Equation (14)) the near-field domain size is such that $2.35(u_6^{(6)}) < \frac{L_0}{2\sqrt{2}w_x} < 2.65(u_7^{(7)})$ and therefore the highest order of AHF2 to be considered is roughly $N = M = 7$.

According to this expansion, the transient near field on π_0 is reconstructed with good accuracy both in the early transient and in the signals tail as shown in Fig. 9.

The angle-frequency transfer function plot, as computed by the proposed Hermite processing at $\phi = 90°$ plane is presented in Fig. 10. The high-pass nature of the antenna is clearly evident as well as the nearly constant group delay at the boresight which indicates a reduced distortion of the transmitted pulse.

Values of transfer function at boresight observation and off the boresight have been further used to regenerate the far field dynamics corresponding to $\tilde{v}_t(\omega) = F[v_t(t)]$ input function according to $\tilde{\boldsymbol{E}}(\boldsymbol{r}, \omega) \propto \tilde{v}_t(\omega)\boldsymbol{\mathcal{H}}^T(\hat{\boldsymbol{r}}, \omega)\frac{e^{jkr}}{r}$. Results in Fig. 11 are compared with reference solutions and it can be appreciated a good reconstruction of the field even when the only h_{00} and h_{20} functions are considered on the boresight observation, and the h_{00} plus h_{11} for off- boresight signals.

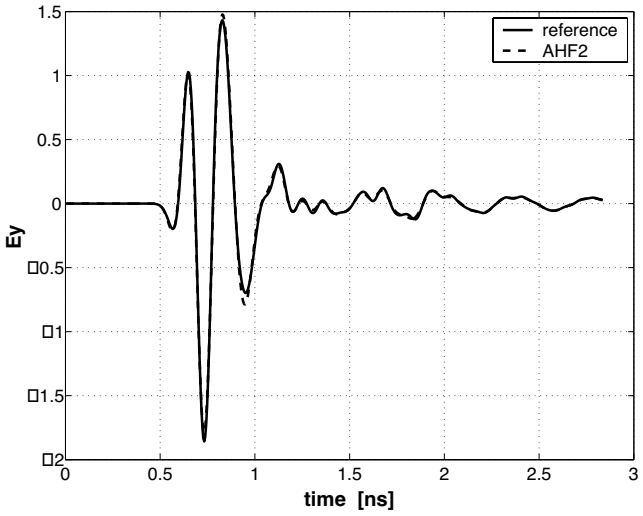

Figure 9. CRH antenna: interpolation of the near-field (in normalized units) on the π_0 plane at point $x_0 = y_0 = 4.5\,\text{cm}$ by the two-dimensional Associate Hermite series $E_y(x_0, y_0, t) = \sum v_{y,mn}(t) h_{mn}(x, y, w)$ with $N = M = 7$.

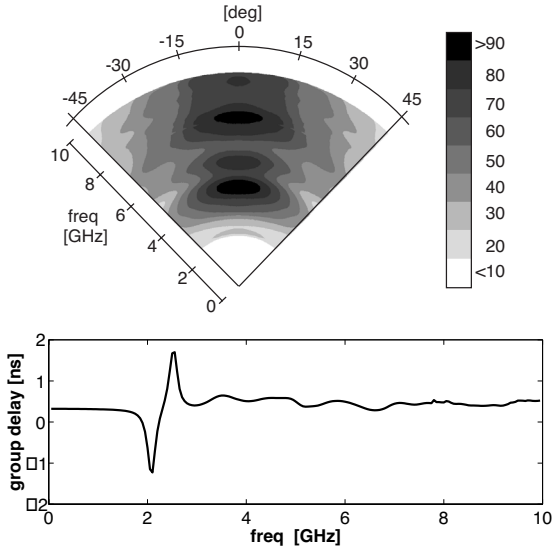

Figure 10. CRH antenna: transfer function (in normalized units) at $\phi = 0°$, amplitude of the θ-component and group delay along the boresight.

5.2. UWB Dipole

An ultra-wideband planar dipole with elliptical branches (Agrawall dipole [22]) is placed in front of a finite reflecting plane (Fig. 12) with the purpose to concentrate the radiation mainly in $z > 0$ half space.

The antenna is sourced by a Gaussian pulse with parameters $T_0 = 24\,\text{ps}$ and $\tau_0 = 130\,\text{ps}$. This kind of geometry provides a hard test for the AHF2 interpolation since, unlike the case of aperture-like antennas, the radiated near-field sensibly spreads on the π_0 plane as the

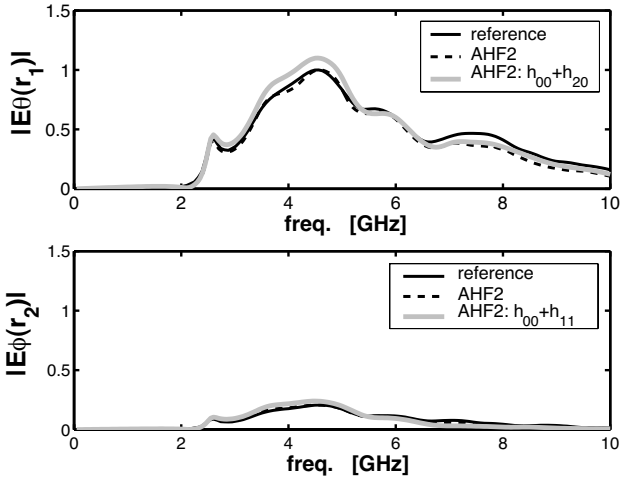

Figure 11. CRH antenna: comparison between reference solution and AHF2 reconstructions for the far-field data (normalized units) at the boresight, $P_1 = (r_1 = 15\,\text{cm},\ \theta = 0^\circ,\ \phi = 0^\circ)$, and off-the-boresight, $P_2 = (r_2 = 48.8\,\text{cm},\ \theta = 18^\circ,\ \phi = 45^\circ)$.

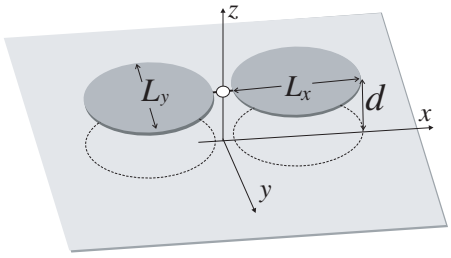

Figure 12. Agrawall dipole: geometry size: $L_x = 5\,\text{cm}$, $L_y = 4.6\,\text{cm}$, $d = 2.4\,\text{cm}$. Reflecting panel size: $20 \times 20\,\text{cm}^2$.

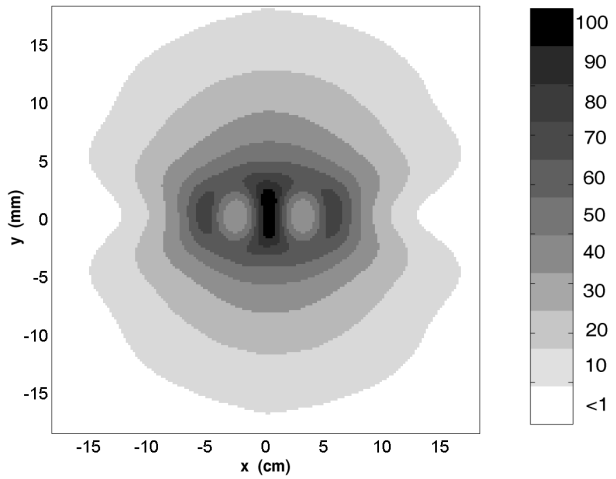

Figure 13. Agrawall dipole: near field energy on the plane π_0 at a distance $z_0 = 18\,\text{mm}$ from the antenna when it is sourced by a gaussian pulse with parameters $To = 24\,\text{ps}$ and $\tau_0 = 130\,\text{ps}$.

time goes on. Departing interference fringes therefore produce a null in front of the antenna gap at some time intervals. As a consequence, it is expected that the radiated energy is less concentrated in front of the antenna (see Fig. 13), the field support on π_0 will enlarge along with the time and a big set of AHF2 could be involved in the field processing.

By placing a square observation plane π_0, of size $L_0 = 40\,\text{cm}$, at a distance $z_0 = 1.8\,\text{cm}$ from the antenna and choosing equal scaling factors $w_x = w_y = 2.46\,\text{cm}$, the maximum order of the AHF2 which could be computed by the Hermite Transform (according to Equation (14)) will be $N = M = 22$. Fig. 14 shows the energy spectrum of the first $n, m < 15$ time-variant interpolation coefficients. As expected, the diagram is less concentrated than in the CRH example and therefore a larger number of terms will be required for an accurate reconstruction of the antenna dynamics. Snapshots of the near-field, interpolated on the π_0 plane by the Hermite base (Fig. 15), show a good agreement with the original data even when the radiated waveforms move far from the domain centre. Some difficulties begin to arise when the wavefront approaches the boundary of the observation plane.

The far-field (Fig. 16) is reconstructed, as in the previous example, with good accuracy up to 4 GHz, (e.g., in the antenna band), after which the reconstructed field presents some discrepancies with the

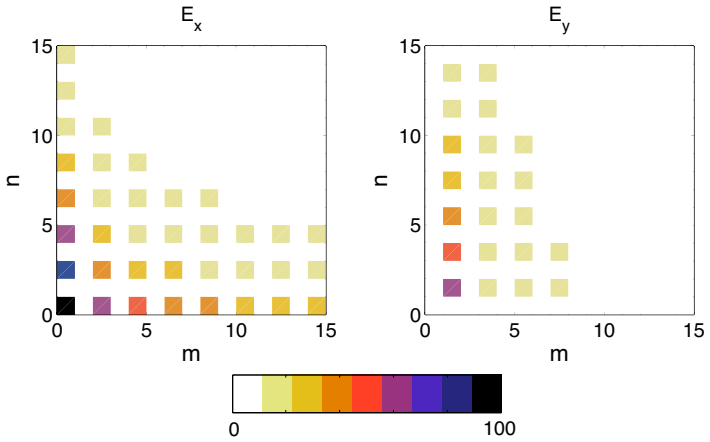

Figure 14. Agrawall dipole: energy spectrum of the Hermite coefficients for near-field interpolation.

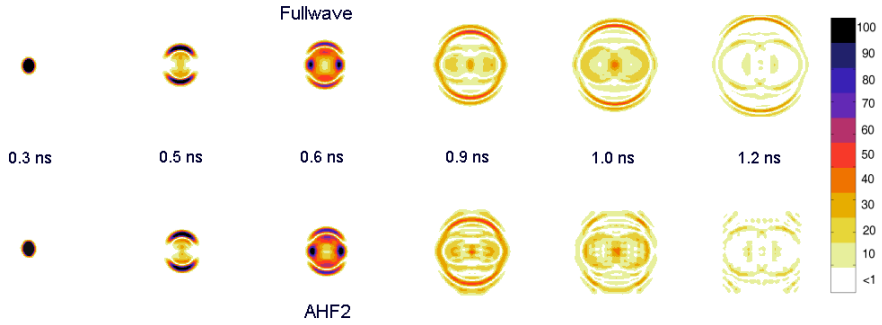

Figure 15. Agrawall dipole: some snapshots of the near field ($|E_x(x, y, t)|$ component) on the observation plane π_0 placed at a distance $z_0 = 18\,\text{mm}$ from the antenna as computed by FDTD (upper line) and interpolated by AHF2s (lower line).

reference data.

The time-domain effective height is computed according to (9) by using the same data of the transfer function. It can be observed in Fig. 17 an approximate second-order derivative behavior of the UWB dipole, e.g., three distinct finite-width pulses with reversed polarity.

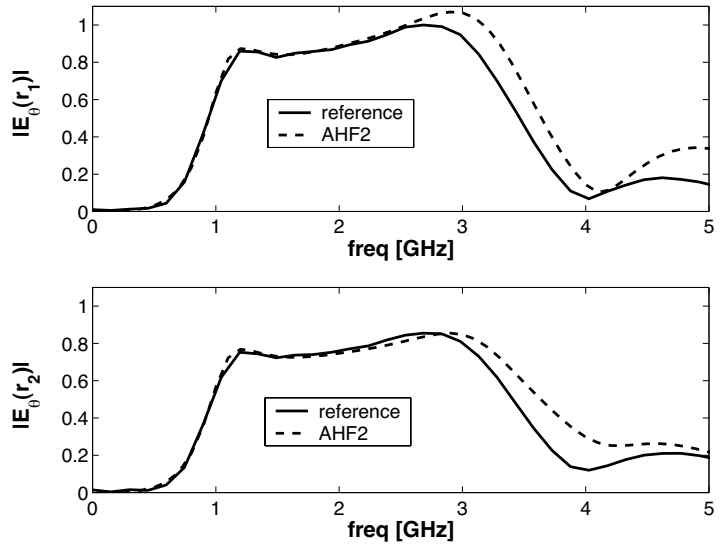

Figure 16. Agrawall dipole: comparison between reference solution and AHF2 reconstructions for the far field $r|E_\theta|$ at angles $(\theta = 0°, \phi = 0°)$ -up- and $(\theta = 12°, \phi = 0°)$ -down. Data in normalized units.

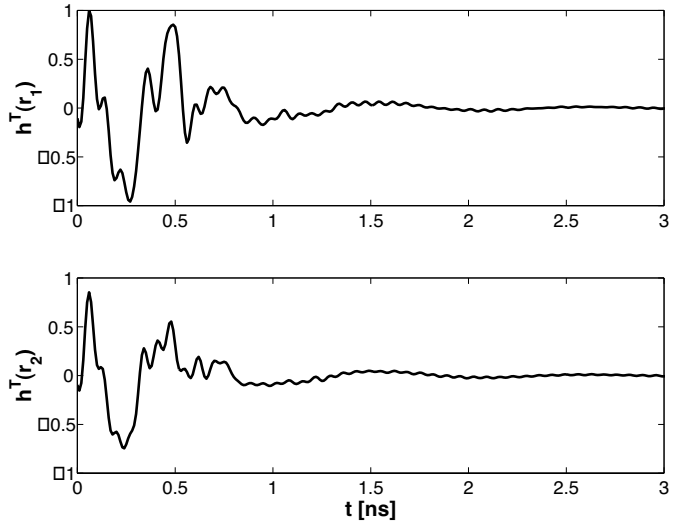

Figure 17. Agrawall dipole: time-domain effective height (in normalized units) at angles $(\theta = 0°, \phi = 0°)$ -up- and $(\theta = 12°, \phi = 0°)$ -down- as computed by AHF2 processing.

6. CONCLUSIONS

A new approximate compact space-time-frequency field representation for moderately-directive UWB antennas has been presented. The use of two-dimensional Associate Hermite functions permits to characterize the time-varying electromagnetic dynamics of the antenna by a small set of scalar data and to express the antenna impulse response and the transfer function by semi-analytical formulas thanks to the Fourier transform isomorphism of such a base. The number of AHF2s to consider, and therefore of the data to store, depends on the antenna size and on the spatial collimation of the radiated field. The Hermite processing required to extract the interpolation coefficients can be introduced into any existing TD code with an automatic selection of the relevant parameters (scaling factor, effective antenna footprint, orders of polynomials), and can be executed at run-time with a modest increase in the computational effort.

The method is really efficient for aperture like-antennas, for which it requires one or two AHF2s to reconstruct the radiated field with good accuracy, but it is useful even for non so directive antennas although a larger number of Hermite functions is needed.

The proposed processing could be applied for both data compression and to define a general interface for the inclusion of the antenna description into a ray-tracing working in the time as well in the frequency domain.

REFERENCES

1. Ghavami, M., L. B. Michael, and R. Kohno, *Ultra-wideband-signals and Systems in Communication Engineering*, Wiley & Sons, England 2004.
2. Marrocco, G., "Modal near-field to far-field transformation for FDTD modelling of aperture antennas," *J. of Electromagn. Waves and Appl.*, Vol. 17, No. 1, 79–98, 2003.
3. Marrocco, G. and M. Ciattaglia, "Ultra-wide band modelling of transient radiation from aperture antennas," *IEEE Trans. Antennas Propagat.*, Vol. 52, No. 10, 2341–2347, Sep. 2004.
4. Kogelnik, H. and T. Li, "Laser beams resonators," *Appl. Opt.*, Vol. 5, No. 10, 1550–1567, Oct. 1966.
5. Arora, R. K. and Z. Lu, "Graphical depiction of the electromagnetic fields of Hermite-Gaussian modes," *IEE Proceed. Microwaves, Antennas and Propagation H*, Vol. 139, No. 4, 369–375, Aug. 1992.

6. Garcia-Munoz, V. and M. A. Muriel, "Hermite-gauss series expansions applied to arrayed waveguide gratings," *IEEE Photonics Technology Letters*, Vol. 17, No. 11, 2331–2333, November 2005.
7. Shen, T., W. Dou, and Z. Sun, "Asymmetrical gauss-hermite beam-mode analysis of the hexagonal horn," *IEEE Transactions on Microwave Theory and Techniques*, Vol. 46, No. 10, 1444–1451, October 1998.
8. Withington, S. and J. A. Murphy, "Analysis of diagonal horns through Gaussian-Hermite modes," *IEEE Trans. Antennas Propagat.*, Vol. 40, No. 2, 198–206, Feb. 1992.
9. Bogush Jr., A. and R. Elkins, "Gaussian field expansions for large aperture antennas," *IEEE Trans. Antennas Propagat.*, Vol. 34, No. 2, 228–243, Feb. 1986.
10. Erteza, I. A. and J. W. Goodman, "A scalar variational analysis of rectangular dielectric waveguides using Hermite-Gaussian modal approximations," *Journal of Lightwave Technology*, Vol. 13, No. 3, 493–506, Mar. 1995.
11. Rao, M. M., T. L. Sarkar, T. Anjali, and R. S. Adve, "Simultaneous extrapolation in time and frequency domains using hermite expansions," *IEEE Trans. Antennas Propagat.*, Vol. 47, No. 6, 1108–1115, June 1999.
12. Martens, J. B., "The Hermite transform-theory," *IEEE Trans.on Acustic Speech and Signal Processing*, Vol. 38, No. 10, 1595–1606, Sept. 1990.
13. Bardati, F., E. Di Giampaolo, A. Durantini, and G. Marrocco, "Vertical antenna near-field computation in complex environmentd by an hybrid method," *Proceedings of Applied Computational Electromagnetics Conference (ACES)*, 975–980, Monterey, USA, 2000.
14. Shlivinski, A., E. Heyman, and R. Kastner, "Antenna characterization in the time domain," *IEEE Trans. Antennas Propagat.*, Vol. 45, No. 7, 1140–1149, June 1997.
15. Ciattaglia, M. and G. Marrocco, "Approximate calculation of time-domain effective height for aperture antennas," *IEEE Trans. Antennas Propagat.*, Vol. 53, No. 3, 1054–1061, Mar. 2005.
16. Yee, K. S., "Numerical solution of initial boundary value problems involving Maxwell's equations in isotropic media," *IEEE Trans. Antennas Propagat.*, Vol. 14, No. 8, 801–806, May 1966.
17. Lo Conte, L. R., R. Merletti, and G. V. Sandri, "Hermite expansion of compact support waveforms: application to

myoelectric signals," *IEEE Trans. Biomed. Eng.*, Vol. 41, No. 12, 1147–1159, Dec. 1994.

18. Marrocco, G. and F. Bardati, "Time-domain macromodel of planar microwave devices by FDTD and moment expansion," *IEEE Trans. Microwave Theory Tech.*, Vol. 49, No. 7, 1321–1328, July 2001.
19. Sarkar, T. K. and O. Pereira, "Using the Matrix Pencil method to estimate the parameters of a sum of complex exponentials," *IEEE Antennas and Propagat. Magazine*, Vol. 37, 48–55, Jan. 1995.
20. Yaghijan, A. D., "An overview of near-field antenna measurements," *IEEE Trans. Antennas Propagat.*, Vol. 34, No. 1, 30–45, Jan. 1984.
21. Press, Q. H., W. T. Vetterling, S. A. Teukolsky, and B. P. Flannery, *Numerical Recipes in C*, 147–157, Cambridge University Press, Cambridge, USA, 1992.
22. Agrawall, N. P., G. Kumar, and K. P. Ray, "Wide-band planar monopole antennas," *IEEE Trans.Antennas Propagat.*, Vol. 46, No. 2, 294–295, Feb. 1998.
23. Soliman, M. S., A. Hirata, T. Morimoto, and Z.-I. Kawasaki, "Numerical and experimental study on three-dimensional localization for ultra-widebandimpulsive noise sources," *J. of Electromagn. Waves and Appl.*, Vol. 19, No. 2, 175–187, 2005.
24. Klemm, M. and G. Troester, "EM energy absorption in the human body tissues due to UWB antennas," *Progress In Electromagnetics Research*, PIER 62, 261–280, 2006.
25. Eldek, A. A., "Numerical analysis of a small ultra wideband microstrip-FED tap monopole antenna," *Progress In Electromagnetics Research*, PIER 65, 59–69, 2006.
26. Eldek, A. A., "Design of double dipole antenna with enhanced usable bandwidth for wideband phased array applications," *Progress In Electromagnetics Research*, PIER 59, 1–15, 2006.